Infrared and visible image fusion based on empirical curvelet transform and phase congruency

[1] Defa Hu and [2] Hailiang Shi

[1] School of Computer Science and Information Engineering, Hunan University of Technology and Business, Changsha 410205, Hunan, China
[2] College of Mathematics and Information Science, Zhengzhou University of Light Industry, Zhengzhou 450000, Henan, China

Received: 20.03.2021

Abstract. We suggest a novel infrared-and-visible image fusion method based on empirical curvelet transform (ECT) and phase congruency (PC). Since the wavelet bases of ECT are not fixed, the ECT is in fact an adaptive multiscale representation method, whereas the PC can measure significance of feature pixels. Then a combination of the ECT and the PC can efficiently extract and retain the features of source images. Our fusion method includes the three following steps: (i) decomposing a source images into ECT coefficients, (ii) fusing low-frequency subbands using the weighted averaging procedure based on log-Gabor energy taken from the PC theory, and fusing high-frequency coefficients using the maximum selection rule based on the PC, and (iii) composing the coefficients of all subbands to form a fused image with the inverse ECT. The experimental results derived on three image pairs demonstrate that our method provides a satisfying visual effect of fusion. Moreover, it outperforms a number of traditional methods in terms of different quantitative metrics.

Keywords: image fusion, infrared images, empirical curvelet transform, phase congruency.

UDC: 004.932

1. Introduction

Image fusion aims at generating a new fused image that complements information concerned with a scene under interest. It has been widely used in object detection, security surveillance, remote sensing, etc. (see Ref. [1]). In particular, a thermal infrared sensor captures mainly the thermal-radiation information of objects in surveillance applications. Then the captured information is not affected by illumination and can easily discover and highlight the targets. However, the infrared image often has a low spatial resolution, while the appearance information is lost since the appearance of objects seldom influences thermal-radiation images [1]. Therefore, it is necessary to compose the thermal radiation information and the appearance information into a single image which is useful for subsequent computer processing.

The methods based on multi-scale transform (MST) are well-known in image fusion methods. Usually, they involve the three following steps: (i) decomposition, (ii) fusion of representation and (iii) reconstruction [2, 3]. Laplacian pyramid (LP), discrete wavelet transform (DWT), shift-invariant DWT (SIDWT), contourlet transform (CT) and nonsubsampled CT (NSCT) are among the known MSTs approaches. Wavelets and their geometric extensions are useful mathematical tools employed in image processing. However, wavelet bases are constructed with a prescribed method corresponding to dyadic scale decomposition. It can prove that these bases are not the best for representing an image [4]. In addition, infrared and visible images have different

characteristics. In an infrared image, thermal-radiation information of a target typically corresponds to higher intensities. In contrast, the appearance information in a visible image is expressed by a gradient, and larger gradients provide details and more salient information [1]. So, it would not be proper to extract different features using the same wavelet bases.

Unlike the traditional MSTs, the wavelet bases of an empirical curvelet transform (ECT) are not fixed. Rather they are dependent on the signals being processed. This makes them optimal for decompositions aimed at extracting salient information. To retain the salient information, one needs that the fused image keep both the thermal-radiation and appearance information. To this end, a novel fusion method based on the ECT is suggested.

The rest of this article is organized as follows. Section 2 presents the preliminaries of basic theories of the ECT and the PC. In Section 3, we describe our fusion method based on the ECT and the PC. Section 4 illustrates the fusion experiments performed on publicly available image pairs. Here a comparison with several traditional fusion methods is elucidated. Finally, the conclusions are drawn in Section 5.

2. Preliminaries

2.1. ECT

Gilles [5] has proposed a 1D empirical wavelet to extract the amplitude modulated−frequency modulated components. Soon afterward Gilles et al. [4] have generalized the above empirical scheme to several existing 2D wavelets. One of the relevant successful schemes is the ECT.

The curvelet transform (CT) has been suggested in Ref. [6]. Its central idea is to construct a filter bank in the Fourier domain. The Fourier representation of a single curvelet is given by

$$\mathcal{F}_2(\psi_j)(\omega,\theta) = 2^{-3j/4} W(2^{-j}\omega) V\left(\frac{2\lfloor j/2 \rfloor \theta}{2\pi}\right), \tag{1}$$

where ψ_j means the wavelet filter at j th scale, $W(r)$ and $V(t)$ are functions defined over compact supports, and (ω,θ) are the polar coordinates. The empirical extension implies detecting the scales and the angles for each polar wedge. Suppose that the number of angular sectors is denoted as N_θ and the number of scales as N_s. The low-pass filter ϕ_1 can be given by

$$\mathcal{F}_2(\phi_1)(\omega) = \begin{cases} 1, if\ |\omega| \le (1-\gamma)\omega^1 \\ \cos\left[\frac{\pi}{2}\beta\left(\frac{1}{2\gamma\omega^1}\left(|\omega| - (1-\gamma)\omega^1\right)\right)\right], if\ (1-\gamma)\omega^1 \le |\omega| \le (1+\gamma)\omega^1 \\ 0, otherwise \end{cases}, \tag{2}$$

where β is an arbitrary function such that $\beta(x) = 0$ if $x \le 0$, $\beta(x) = 1$ if $x \ge 1$ and $\beta(x) + \beta(1-x) = 1$ ($\forall x \in [0,1]$). The parameter γ ensures that the two consecutive transition areas do not overlap. As with the CT, the polar wedge ψ_{nm} (with n being the scale index and m the angular index) depends on the radial window W_n. In case of $n \ne N_s - 1$, the latter is given by

$$W_n(\omega) = \begin{cases} 1, if\ (1+\gamma)\omega^n \le |\omega| \le (1-\gamma)\omega^{n+1} \\ \cos\left[\frac{\pi}{2}\beta\left(\frac{1}{2\gamma\omega^{n+1}}\left(|\omega| - (1-\gamma)\omega^{n+1}\right)\right)\right], if\ (1-\gamma)\omega^{n+1} \le |\omega| \le (1+\gamma)\omega^{n+1} \\ \sin\left[\frac{\pi}{2}\beta\left(\frac{1}{2\gamma\omega^{n}}\left(|\omega| - (1-\gamma)\omega^{n}\right)\right)\right], if\ (1-\gamma)\omega^{n} \le |\omega| \le (1+\gamma)\omega^{n} \\ 0, \quad \text{otherwise} \end{cases}. \tag{3}$$

If we have $n = N_s - 1$, then

$$W_{N_s-1}(\omega) = \begin{cases} 1, if\ (1+\gamma)\omega^{N_s-1} \le |\omega| \\ \sin\left[\frac{\pi}{2}\beta\left(\frac{1}{2\gamma\omega^{N_s-1}}\left(|\omega| - (1-\gamma)\omega^{N_s-1}\right)\right)\right], if\ (1-\gamma)\omega^{N_s-1} \le |\omega| \le (1+\gamma)\omega^{N_s-1} \\ 0, \quad \text{otherwise} \end{cases}. \quad (4)$$

Finally, the polar window V_m is described as

$$V_m(\theta) = \begin{cases} 1, if\ \theta^m + \Delta\theta \le \theta \le \theta^m - \Delta\theta \\ \cos\left[\frac{\pi}{2}\beta\left(\frac{1}{2\Delta\theta}\left(\theta - \theta^{m+1} + \Delta\theta\right)\right)\right], if\ \theta^{m+1} - \Delta\theta \le \theta \le \theta^{m+1} + \Delta\theta \\ \sin\left[\frac{\pi}{2}\beta\left(\frac{1}{2\Delta\theta}\left(\theta - \theta^{m} + \Delta\theta\right)\right)\right], if\ \theta^{m} - \Delta\theta \le \theta \le \theta^{m} + \Delta\theta \\ 0, \quad \text{otherwise} \end{cases}, \quad (5)$$

where $\theta^{N_\theta+1} = \theta^1 + \pi$.

2.2. PC and log-Gabor energy

The PC has been defined by Morrone et al. [7]. For 2D images, the concept has been improved using log-Gabor wavelet filters for each pixel, whereas the implementation has been specified in Refs. [8, 9]. The 2D version is defined as

$$PC_2(x,y) = \frac{\sum_o \sum_n W_o(x,y)\lfloor A_{no}(x,y)\Delta\Phi_{no}(x,y) - T_o \rfloor}{\sum_o \sum_n A_{no}(x,y) + \varepsilon}. \quad (6)$$

Here o corresponds to orientations, n is the index of scales, $W_o(x,y)$ the weight function, $A_{no}(x,y)$ the amplitude, $\Delta\Phi_{no}(x,y)$ the phase-deviation measure, T_o the estimated noise influence, and ε a small constant.

In its implementation, the log-Gabor filter $\mathcal{G}(u,v)$ allows for constructing the filters with arbitrarily large bandwidths. The definition is as follows [10]:

$$\mathcal{G}(u,v) = \exp\left(-\frac{\left(\ln\frac{\sqrt{u^2+v^2}}{\omega}\right)^2}{2\left(\ln\sigma_1\right)^2}\right) \cdot \exp\left(-\frac{\left(\arctan\frac{u}{v} - \alpha\right)^2}{2\sigma_2^2}\right), \quad (7)$$

where α and σ_2 are the parameters of angular interval, σ_1 is set to be 0.55 to obtain two bandwidths, and ω is the central frequency. Then, a series of $s_{no}(x,y)$ and $h_{no}(x,y)$ parameters (i.e., the real and imaginary parts of the output, respectively) can be obtained with different scales of the log-Gabor filter:

$$s_{no}(x,y) + ih_{no}(x,y) = \mathcal{F}^{-1}\{\mathcal{F}[I(x,y)]\mathcal{G}(u,v)\}. \quad (8)$$

Here (x,y) denotes the space coordinates, (u,v) are the frequency coordinates, and $\mathcal{F}$ and $\mathcal{F}^{-1}$ are respectively the Fourier and inverse Fourier transforms.

The local energy for a given orientation can be obtained via

$$E_o(x) = \sqrt{\left(\sum s_{no}(x)\right)^2 + \left(\sum h_{no}(x)\right)^2}. \quad (9)$$

Eventually, the log-Gabor energy is defined as

$$\begin{aligned} LGE(x,y) &= A_{no}(x,y)\Delta\Phi_{no}(x,y) \\ &= s_{no}(\mathrm{x},\mathrm{y})\bar{\phi}_{so}(x,y) + h_{no}(x,y)\bar{\phi}_{ho}(x,y) - \left|s_{no}(\mathrm{x},\mathrm{y})\bar{\phi}_{ho}(x,y) - h_{no}(x,y)\bar{\phi}_{so}(x,y)\right|, \end{aligned} \quad (10)$$

where

$$\bar{\phi}_{so}(x) = \sum s_{no}(x) / E_o(x), \tag{11}$$

$$\bar{\phi}_{ho}(x) = \sum h_{no}(x) / E_o(x). \tag{12}$$

The weight function $W_o(x)$ used in Eq. (1) is given by the relation

$$W_o(x,y) = \frac{1}{1+\exp\left[-\gamma(\chi_0(x,y)-c)\right]}, \tag{13}$$

where γ and c are constants, and $\chi_0(x,y)$ is given by

$$\chi_0(x,y) = \frac{1}{N}\left(\frac{\sum A_{no}(x,y)}{A_{\max}(x,y)+\varepsilon}\right). \tag{14}$$

Here N denotes the total number of scales and $A_{\max}(x,y)$ is the maximum amplitude.

3. Our fusion method

Based on the above theory, the ECT and the 2D PC can be efficiently applied to the problem of image fusion. The ECT can provide adaptive representation of source images, while the 2D PC can measure a significance of feature points [9]. Then the combination of the ECT and the 2D PC would extract efficiently the features of the source images.

The fusion method based on the ECT and the 2D PC includes the following three steps.

(1) Decompose both source images, an infrared image A and a visible image B, using the ECT. Then the coefficients of the two images are obtained as $\left\{L^{A_{i,j}}, H_{k,\theta}^{A_{i,j}}\right\}$ and $\left\{L^{B_{i,j}}, H_{k,\theta}^{B_{i,j}}\right\}$, where L represents the low-frequency coefficient and $H_{k,\theta}$ denote the high-frequency subband coefficients for decompositions in k levels and θ directions.

(2) Compose the coefficients for the low- and high-frequency subbands basing on some rules:

(a) The low-frequency subband aggregates most of the energy of image, which indicates that the averaging rule weighted by the energy could be suitable for fusing. In this work, we obtain the energy definition in an alternative way, using the theory of PC. In other words, the log-Gabor energy is used as an activity measure to merge the low-frequency coefficients. The log-Gabor energies of the low-frequency subbands for the A and B images are denoted as $LGE^A(i,j)$ and $LGE^B(i,j)$, respectively. The adopted weighted-averaging rule based on the log-Gabor energy can be represented as follows:

$$w_{i,j} = \frac{LGE^A(i,j)+C}{LGE^A(i,j)+LGE^B(i,j)+C}, \tag{15}$$

$$L^{F_{i,j}} = w_{i,j}\cdot L^{A_{i,j}} + \left(1-w_{i,j}\right)\cdot L^{B_{i,j}}, \tag{16}$$

where C is a small constant, $w_{i,j}$ the decision map, and $L^{F_{i,j}}$ the fused low-frequency coefficient.

(b) The high-frequency subbands reflect mainly the information on image details, and the PC is suitable to measure the significance of feature pixels. Therefore we adopt the maximum-selection rule based on the PC_2 value in order to compose the high-frequency coefficients:

$$H_{k,\theta}^{F_{i,j}} = \begin{cases} H_{k,\theta}^{A_{i,j}}, if\ PC_2\left(H_{k,\theta}^{A_{i,j}}\right) > PC_2\left(H_{k,\theta}^{B_{i,j}}\right) \\ H_{k,\theta}^{B_{i,j}}, \quad \text{otherwise} \end{cases}. \tag{17}$$

(3) Use the wavelets obtained from the ECT on the infrared image to perform the inverse ECT on the fused coefficients and form a fused image F.

4. Experimental results

Now we test the performance of our fusion method using three publicly available image pairs. Moreover, we compare the appropriate results with those obtained using the traditional fusion methods. These are the fusion methods based upon LP [11], DWT [11], SIDWT [11], CT and NSCT.

4.1. Setups of fusion methods

For the MST-based methods mentioned above, classical steps discussed in Section 1 are followed. Besides, a classical averaging scheme is employed for the corresponding low-frequency subbands. The maximum-selection scheme is used for the high-frequency subbands. The decomposition levels are set to be 3. The codes of the LP-, DWT- and SIDWT-based methods are obtained from a Rockinger image-fusion toolbox [11]. For the CT and NSCT methods, we use the wavelet bases '9-7' and 'pvka' respectively on the pyramid decomposition stage and the directional decomposition stage.

4.2. Fusion metrics

In our experiments, both qualitative and quantitative comparisons are conducted on different fused images. The quantitative evaluation is performed using the five metrics: standard deviation (SD), average gradient (AG), spatial frequency (SF), information entropy (IE), and mutual information (MI). The definitions of these metrics are given below:

$$\begin{aligned} &SD(F)=\left[\frac{1}{mn}\sum_{i=1}^{m}\sum_{j=1}^{n}(F(i,j)-u)\right]^{\frac{1}{2}},\\ &u=\frac{1}{mn}\sum_{i=1}^{m}\sum_{j=1}^{n}F(i,j) \end{aligned} \tag{18}$$

(with $F(i,j)$ being the pixel intensity of the fused image),

$$AG(F)=\frac{1}{(m-1)(n-1)}\times\sum_{i=1}^{m-1}\sum_{j=1}^{n-1}\left[\left(F(i,j)-F(i+1,j)\right)^2+\left(F(i,j)-F(i,j+1)\right)^2\right]^{\frac{1}{2}}, \tag{19}$$

$$IE(F)=-\sum_{i=0}^{L-1}p(i)\log_2 p(i) \tag{20}$$

(with $p(i)$ representing the probability of gray value i of pixel and L being the total number of gray level),

$$\begin{cases} SF(F)=\sqrt{RF^2+CF^2}\\ RF=\left(\frac{1}{m(n-1)}\sum_{i=1}^{m}\sum_{j=1}^{n-1}(F(i,j+1)-F(i,j))^2\right)^{\frac{1}{2}}\\ CF=\left(\frac{1}{(m-1)n}\sum_{i=1}^{m-1}\sum_{j=1}^{n}(F(i+1,j)-F(i,j))^2\right)^{\frac{1}{2}} \end{cases} \tag{21}$$

(with RF and CF being respectively the row and column frequencies),

$$MI(I,F)=\sum_{i_1=1}^{L}\sum_{i_2=1}^{L}h_{I,F}(i_1,i_2)\log_2\frac{h_{I,F}(i_1,i_2)}{h_I(i_1)h_F(i_2)} \tag{22}$$

(with $h_{I,F}$ denoting the jointly normalized histogram of the images I and F, h_I and h_F being the normalized histograms of I and F, and i_1 and i_2 representing the pixel values of I and F, respectively).

Finally, the MI used by us is the average value:

$$MI(A,B,F)=\tfrac{1}{2}\big(MI(A,F)+MI(B,F)\big). \tag{23}$$

4.3. Fusion results and comparisons

To get an intuitive impression of the performance of our fusion method, we have performed the first experiment on the infrared-and-visible image pair ‘e518’ with the size 512×512 (see Fig. 1a,b). Fig. 1c–h show the appropriate fused images obtained with different fusion methods known from the literature. It is evident that each of the methods provides somewhat different though roughly similar visual perceptions. However, the fused image shown in Fig. 1h, which has been obtained with our method, is much clearer than the other images. Similar to the original infrared image, it reveals high intensity, which is beneficial when representing the image features.

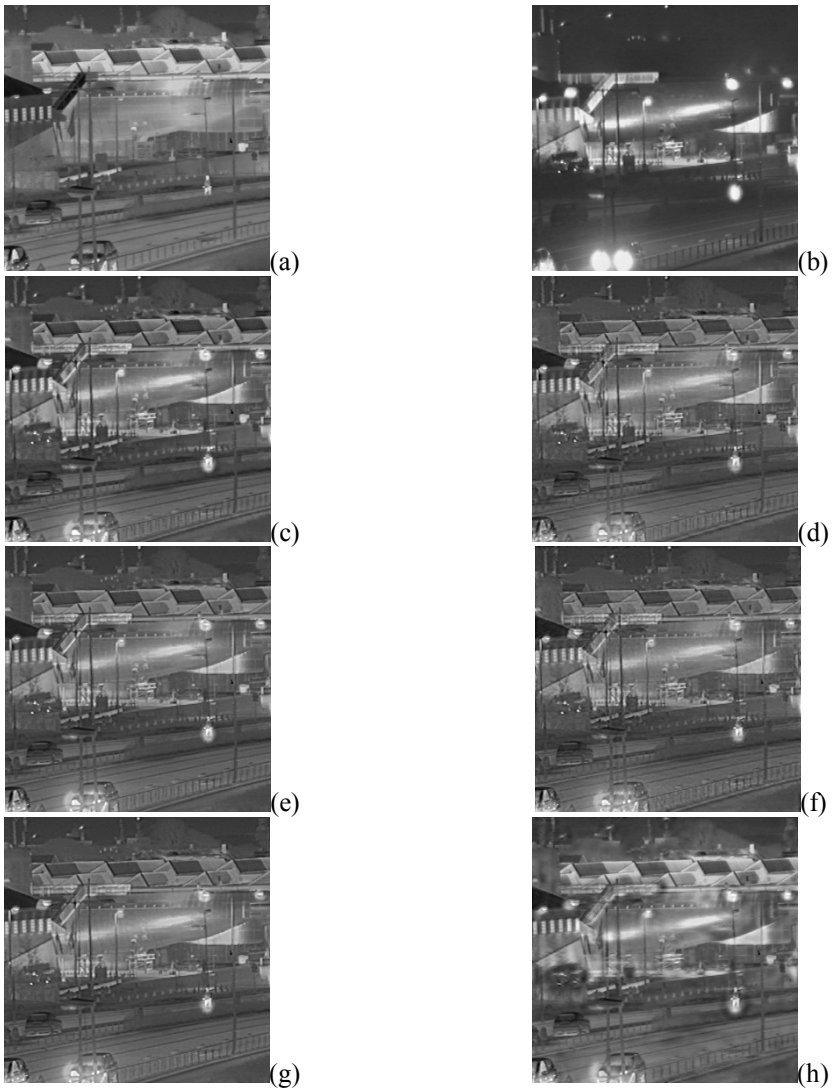

Fig. 1. Infrared and visible source images ‘e518’ and the corresponding fused images: (a) infrared source image, (b) visible source image, and (c)–(h) fused images obtained using the fusion methods based on LP, DWT, SIDWT, CT and NSCT, and our fusion method, respectively.

The second experiment has been performed on the image pair ‘7118a’ with the size 512×512. Fig. 2a–h display the appropriate source and fused images. When compared with the traditional fusion methods, our method takes a lead in the visual effects and preserves the information on details. Although there are shadows in the sky, the people, the ship, the coastline, and the boundary of the sea and sky in the image are prominent.

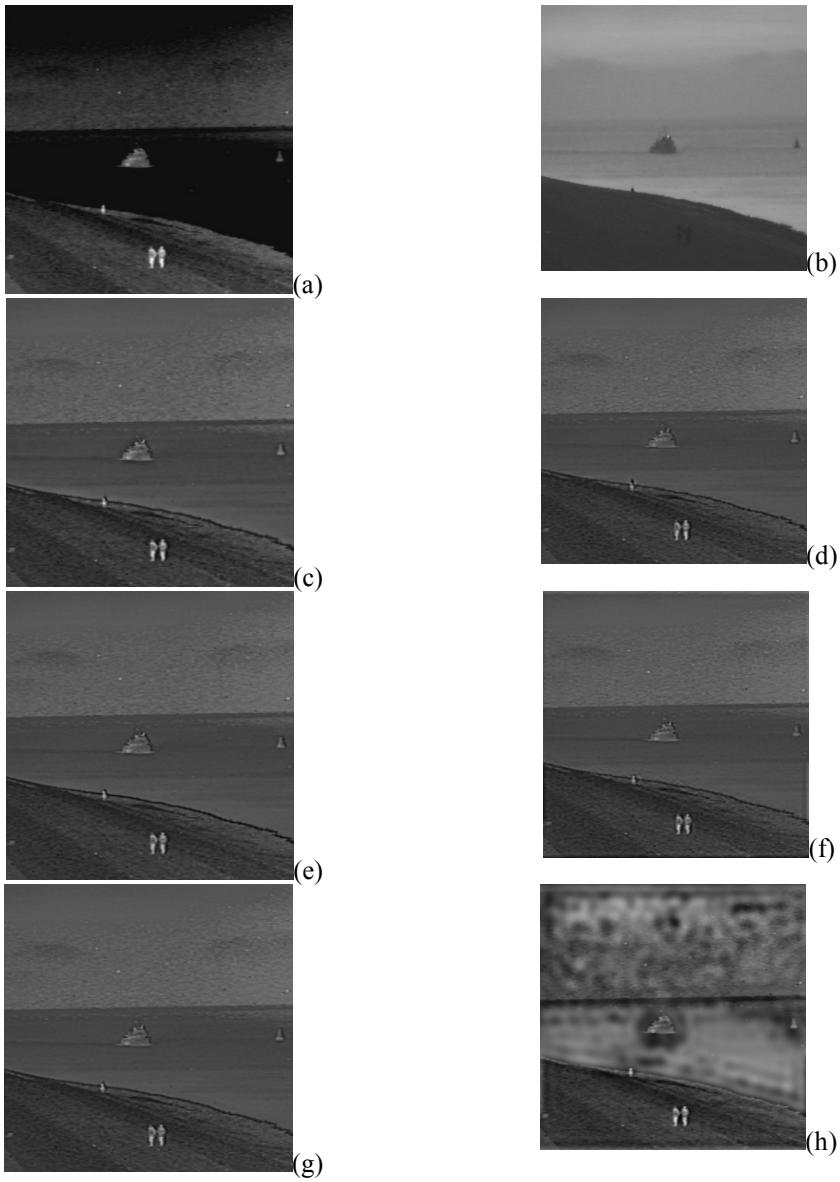

Fig. 2. Infrared and visible source images '7118a' and the corresponding fused images: (a) infrared source image, (b) visible source image, and (c)−(h) fused images obtained using the fusion methods based on LP, DWT, SIDWT, CT and NSCT, and our fusion method, respectively.

To verify further our method, we have also conducted the experiment with a pair of multimodal medical images with the size 256×256 (see Fig. 3a,b). In particular, Fig. 3a displays a computed tomography image, which represents mainly the information concerned with bones. Fig. 3b is a magnetic resonance image, which reflects clearly the information on soft tissues. The fused images obtained with different fusion methods are displayed in Fig. 3c−h. One can conclude that the intensities of the brain tissue regions in Fig. 3c−g are lower than that seen in Fig. 3b, while the image in Fig. 3h shares a similar intensity with the source images. This is why our fusion method works better in preserving the original visual information.

The quantitative comparison of different fusion methods applied to the above three image pairs is illustrated in Table 1. Here the best figures are marked in bold for each metric (i.e., for each column).

Following from the above data, one concludes that, in most of cases, our fusion method provides the best results for the metrics SD, AG, SF, IE and MI. Although it does not yield the best parameters for a few experiments and a few parameters (e.g., the SF data for the 'e518a' pair, the MI data for the '7118a' pair, and the SF data for the medical images), there are no significant differences between the parameters of our method and the best parameters. Hence, we believe that the performance of our method in these exceptional cases is almost the same as the performance of its best rivals.

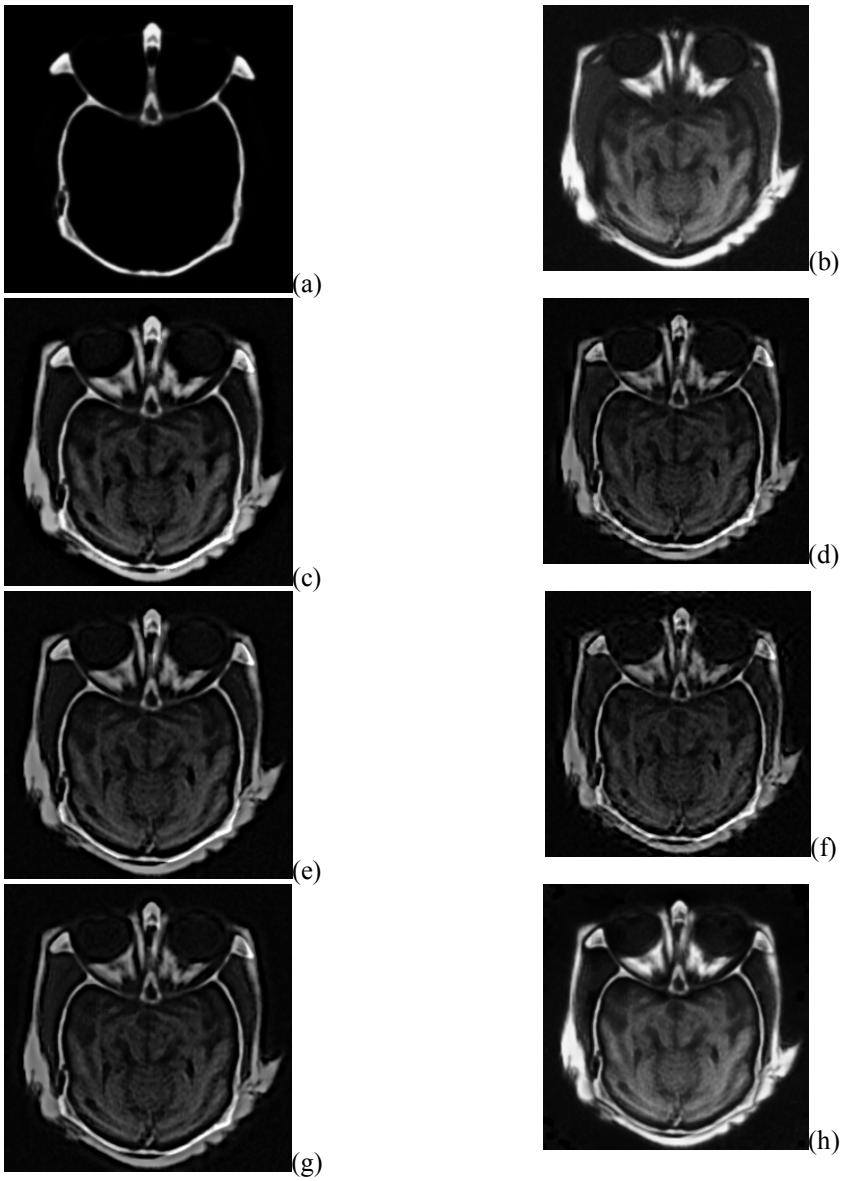

Fig. 3. Medical source images and the corresponding fused images: (a) computed tomography image, (b) magnetic resonance image, and (c)−(h) fused images obtained using the fusion methods based on LP, DWT, SIDWT, CT and NSCT, and our fusion method, respectively.

Issuing from the experimental results, the conclusion can be drawn that our method preserves well both the thermal-radiation information and the appearance information, i.e. it highlights the most important information on the target. Moreover, our method outperforms the traditional fusion methods in both qualitative and quantitative characteristics.

Table 1. Quantitative comparison of fusion results obtained for the images ‘e518’ and ‘7118a’ and the medical images.

Image	Method	$SD(F)$	$AG(F)$	$SF(F)$	$IE(F)$	$MI(A,B,F)$
e518	LP	0.1437	0.0519	**0.0496**	7.0598	0.8428
	DWT	0.1311	0.0471	0.0473	6.9458	0.7869
	SIDWT	0.1331	0.0479	0.0472	6.9574	0.8629
	CT	0.1304	0.0468	0.0474	6.9511	0.7654
	NSCT	0.1293	0.0465	0.0458	6.9232	0.8310
	our method	**0.1482**	**0.0540**	0.0444	**7.1104**	**0.8759**
7118a	LP	0.0702	0.0239	0.0203	6.1023	0.8068
	DWT	0.0673	0.0228	0.0193	6.0355	0.8329
	SIDWT	0.0684	0.0232	0.0203	6.0558	**0.8854**
	CT	0.0695	0.0234	0.0201	6.0878	0.7404
	NSCT	0.0670	0.0227	0.0190	6.0268	0.8750
	our method	**0.1079**	**0.0398**	**0.0211**	**6.7877**	0.3487
medical	LP	0.2022	0.0701	**0.0768**	6.1477	0.3093
	DWT	0.1635	0.0558	0.0712	6.1780	0.2777
	SIDWT	0.1702	0.0586	0.0737	6.0855	0.3010
	CT	0.1600	0.0547	0.0708	6.2897	0.2659
	NSCT	0.1600	0.0550	0.0692	6.1931	0.2954
	our method	**0.2268**	**0.0816**	0.0699	**6.8854**	**0.3274**

5. Conclusion

In the present study, a novel fusion method based on the ECT and the PC approaches has been developed. The wavelet bases of the ECT are not fixed, whereas the PC is a dimensionless quantity which can measure the significance of feature pixels. In the fusion process, our fusion algorithm relies on the weighted averaging rule based upon the log-Gabor energy for the low-frequency subbands and on the maximum selection rule based upon the PC for the high-frequency subbands.

The performance of our method has been tested on three image pairs. It has been compared with a number of traditional fusion methods, which are based on LP, DWT, SIDWT, CT and NSCT approaches. We conclude from the fusion results that our method outperforms the other methods in both visual perception and different quantitative measures.

References

1. Jiayi Ma, Chen Chen, ChangLi, Jun Huang, 2016. Infrared and visible image fusion via gradient transfer and total variation minimization. Inform. Fus. **31**: 100−109.
2. Yang B and Li S, 2012. Pixel-level image fusion with simultaneous orthogonal matching pursuit. Inform. Fus. **13**: 10−19.
3. Piella G, 2003. A general framework for multiresolution image fusion: from pixels to regions. Inform. Fus. **4**: 259−280.
4. Gilles J, Tran G and Osher S, 2014. 2D empirical transforms. wavelets, ridgelets, and curvelets revisited. SIAM J. Imag. Sci. **7**: 157−186.
5. Gilles J, 2013. Empirical wavelet transform. IEEE Trans. Sign. Process. **61**: 3999−4010.
6. Emmanuel J C and Donoho D L, 2000. Curvelets − a surprisingly effective nonadaptive representation for objects with edges. Astron. Astrophys. **283**: 1051−1057.

7. Morrone M C and Owens R A, 1987. Feature detection from local energy. Pattern Recogn. Lett. **6**: 303−313.
8. Kovesi P, 1999. Image features from phase congruency. J. Comp. Vis. Res. **1**: 115−116.
9. Kovesi P, 2000. Phase congruency: a low-level image invariant. Psychol. Res. **64**: 136−148.
10. Zhan K, 2015. Multifocus image fusion using phase congruency. J. Electron. Imag. **24**: 033014.
11. http://www.metapix.de/toolbox.htm.
12. Cvejic N, Seppanen T and Godsill S J, 2009. A nonreference image fusion metric based on the regional importance measure. IEEE J. Sel. Top. Sign. Process. **3**: 212−221.

Defa Hu and Hailiang Shi. 2021. Infrared and visible image fusion based on empirical curvelet transform and phase congruency. Ukr.J.Phys.Opt. **22**: 128 – 137.
doi: 10.3116/16091833/22/3/128/2021

Анотація. *Запропоновано новий метод злиття інфрачервоних і видимих зображень, заснований на емпіричному керблет-перетворенні (ЕКП) і фазовій конгруентності (ФК). Оскільки бази вейвлетів ЕКП не є фіксованими, то ЕКП фактично є адаптивним методом багатомасштабного представлення, тоді як ФК може вимірювати значущість піксельних ознак. Тоді поєднання ЕКТ і ПК дасть змогу ефективно видобувати та зберігати особливості вихідних зображень. Наш метод злиття включає такі три етапи: (1) розкладання вихідних зображень на коефіцієнти ЕКП; (2) злиття низькочастотних піддіапазонів за допомогою зваженої процедури усереднення на основі лог-габорівської енергії, взятої з теорії ФК, і злиття високочастотних коефіцієнтів із використанням правила максимального вибору, заснованого на ПК; (3) складання коефіцієнтів усіх піддіапазонів для формування злитого зображення за допомогою зворотного ЕКП. Експериментальні результати, одержані на трьох парах зображень, демонструють, що наш метод забезпечує задовільний візуальний ефект злиття. Більше того, він перевершує результати низки традиційних методів з точки зору різних кількісних показників.*